Title

Scaling the impacts of pore-scale characteristics on unstable supercritical CO2-water drainage using a complete capillary number

Authors

Chang, Chun
Kneafsey, Timothy J
Zhou, Quanlin
et al.

Publication Date

2019-07-01

DOI

10.1016/j.ijggc.2019.04.010

Scaling the Impacts of Pore-Scale Characteristics on Unstable Supercritical CO_2-Water Drainage Using a Complete Capillary Number

Chun Chang [1, 2,*], Timothy J. Kneafsey[2], Quanlin Zhou[2], Mart Oostrom[3], Yang Ju[1, 4]

[1] State Key Laboratory of Coal Resources and Safe Mining, China University of Mining & Technology (Beijing), Beijing 100083, China

[2] Energy Geosciences Division, Lawrence Berkeley National Laboratory, Berkeley, CA 94720, USA.

[3] Energy and Environment Directorate, Pacific Northwest National Laboratory, 902 Battelle Boulevard, P.O. Box 999, MSIN K8-96, Richland, Washington 99352, USA. Now at INTERA, Inc, Richland, WA.

[4] State Key Laboratory for Geomechanics and Deep Underground Engineering, China University of Mining & Technology, No 1, University Avenue, Xuzhou 221006, P. R. China

[*]Corresponding author. *E-mail address*: chunchang@lbl.gov

Abstract: Geological carbon storage in deep aquifers involves displacement of resident brine by supercritical CO_2 ($scCO_2$), which is an unstable drainage process caused by the invasion of less viscous $scCO_2$. The unstable drainage is greatly complicated by aquifer heterogeneity and anisotropy and regarded as one of the key factors accounting for the uncertainty in storage capacity estimates. The impacts of pore-scale characteristics on the unstable drainage remain poorly understood. In this study, $scCO_2$ drainage experiments were conducted at 40 °C and 9 MPa using a homogeneous elliptical micromodel with low or high anisotropy, a homogeneous/isotropic hexagonal micromodel, and a heterogeneous sandstone-analog micromodel. Each initially water-saturated micromodel was invaded by $scCO_2$ at different rates with $logC_a$ (the capillary number) ranging from −7.6 to −4.4, and $scCO_2$/water images were obtained. The measured CO_2 saturations in these centimeter-scale micromodels vary considerably from 0.08 to 0.93 depending on the pore-scale characteristics and capillary number. It was also observed that $scCO_2$ drainage follows the classic flow-regime transition from capillary fingering through crossover to viscous fingering for either of the low-anisotropy elliptical and heterogeneous micromodels, but with disparate crossover zones. The crossover zones of $scCO_2$ saturation were then unified with the minimum $scCO_2$ saturation occurring at $logC_a^* = -4.0$ using the *complete capillary number* (C_a^*) that considers pore characteristics. For the hexagonal and the high-anisotropy elliptical micromodels, a monotonic increase in $scCO_2$ saturation with increasing C_a^* (without crossover) was observed. It appears that the complete capillary number is more appropriate than the

classic capillary number when characterizing flow regimes and CO_2 saturation in different pore networks.

Keywords: Geological carbon storage, Micromodel, Drainage fingering, Pore characteristics, Capillary number, Complete capillary number

1. Introduction

Carbon capture and storage (CCS) has been considered as an effective technology to reduce greenhouse gas emissions into the atmosphere (IPCC, 2005). A number of laboratory experiments have been conducted under reservoir conditions with natural rock samples to (1) investigate the fundamentals of displacement between supercritical CO_2 ($scCO_2$) and brine and (2) provide parameter measurements for aquifer-scale storage capacity/efficiency estimation (Bennion and Bachu, 2008; Zhang et al., 2011a; Krevor et al., 2012; Pini et al., 2012; Berg and Ott, 2012; Akbarabadi et al., 2013; Chang et al., 2013, 2014, 2016, 2017, 2019; Tsuji et al., 2016). At the laboratory scale (pore and core scales), the storage efficiency is represented by CO_2 saturation (the volumetric fraction of pore space filled by CO_2) in the pore (Bachu, 2015). A wide range of CO_2 saturation measured in laboratory has been reported with a factor of ~20 among 29 sandstone and carbonate rock samples after $scCO_2$ drainage and brine imbibition (Bennion and Bachu, 2010; Bachu, 2013). Core-flooding experiments from Chang et al. (2013) showed the non-uniform displacement between $scCO_2$ and water in two low-permeability sandstone cores, resulting in the variation of CO_2 saturation measured. The variability in these laboratory measurements may attribute to the uncertainty of some key parameters used in estimating the aquifer-scale storage capacity and efficiency.

One of the major reasons for the large variability in measured CO_2 saturation after $scCO_2$ drainage is unstable $scCO_2$ displacement fingering due to the low viscosity of $scCO_2$ relative to formation brine (with a typical ratio: 1 to 20), which is considerably affected by pore geometries (Zhang et al., 2011a,b; Berg and Ott., 2012; Wang, et al., 2012). When CO_2 saturation is determined from an experiment subject to unstable displacement fingering, the measurements are only volume-averaged effective properties limited to the specific experimental conditions, sample size and pore characteristics, and saturation distribution in the experiment (Berg and Ott., 2012).

Since the 1950s, the nature of two-phase displacement instability has been characterized by the *classic capillary number* (C_a) that represents the *relative* effect of viscous forces versus interfacial forces acting across an interface between two immiscible liquids. The classic capillary number, in its original form: $\mu \times \overline{u} / \sigma$, was used to interpret the fingering geometry of air in experiments of air displacing glycerine in a Hele-Shaw cell by Saffman and Taylor (1958). In this definition, μ is the viscosity, $\overline{u}$ is the average Darcy velocity of the injected fluid, and σ is the interfacial tension between the injected and resident fluid. C_a, along with the viscosity ratio (*M*) defined as the ratio of viscosities of the displacing (non-wetting) and displaced (wetting) fluids, has been used to characterize the pore-scale regimes of capillary fingering, viscosity fingering, and crossover in the transition by Lenormand et al. (1988). They also pointed out that the specific boundaries delineating capillary and viscous fingering on the $logC_a - logM$ phase diagram might depend on pore geometry. Recent experimental and modeling results showed the fingering regimes in similar and different pore-networks, and the effect of small variations/randomness in pore geometry on different displacement regimes and CO_2 saturation (Xu et al., 1998;

Ferer et al., 2004, 2005, 2007, 2011; Zhang et al., 2011b; Wang et al., 2012; Cottin et al., 2010; Bandara et al., 2013). Some researchers who use the percolation theory have also reported that it is necessary to modify the traditional, classic capillary number with length scales corresponding to viscous and capillary forces (Wilkinson, 1986; Toussaint et al., 2012) and the size of non-wetting phase (i.e., scCO_2 and oil) clusters (Armstrong et al., 2014). Zheng et al. (2017) summarized the experimental and numerical results published in last three decades (Lenormand et al., 1988; Zhang et al., 2011b; Wang et al., 2012; DeHoff et al., 2012), and clearly presented a disparate relationship between the non-wetting fluid saturation and C_a, and the varying phase boundaries determined from different studies. Hu et al. (2017, 2018) investigated the wettability effects on drainage fingerings in a homogeneous pore-network with cylindrical silicon posts through micromodel experiments and a theoretical model. However, the impacts of pore-scale characteristics on unstable drainage mechanisms remain poorly understood, and the observed disparate relationship between the non-wetting fluid saturation and C_a should be normalized by including the pore-scale characteristics.

In this study, we (1) investigate the effects of pore characteristics such as pore-throat aspect ratio, pore-network anisotropy and heterogeneity on displacement regimes, and (2) re-scale the observed disparate relationship between CO_2 saturation and capillary number by using a *complete capillary number* that accounts for pore characteristics. Different pore characteristics were represented by four micromodels and the flow regimes were investigated by drainage experiments with scCO_2 under a broad range of injection rates.

2. Materials and Methods

In this section, four micromodels were selected to investigate the effects of pore characteristics on $scCO_2$-brine drainage (see Figure 1 and Table 1). The micromodels represent four typical features that may be encountered in subsurface porous media: heterogeneous sandstone-analog (#1), slightly anisotropic but homogeneous (#2), highly anisotropic (#3), and isotropic with a high pore-throat aspect ratio (#4).

2.1 Micromodels

Figure 1 shows the four micromodels used in this study, with pore space shown in white and silicon posts in black. These were fabricated by etching a silicon wafer using microfabrication methods involving standard photolithography, coupled plasma-deep reactive ion etching (ICP-DRIE), thermal oxidation, and anodic bonding (Willingham et al., 2008; Zhang et al., 2011a,b; Wang et al., 2012; Chomsurin and Werth, 2003). The pore network of Micromodel #1 was converted from section micrographs of a Mt. Simon sandstone core extracted from the injection well of the Illinois Basin - Decatur project (Senel et al., 2014). The porous-medium portion consists of nine identical sub-images in a 3 × 3 array and features three large pore channels (see the red solid lines in Figure 1). A Local Thickness plugin in ImageJ software (Hildebrand and Rüesgsegger, P., 1996; Rasband, 1997-2019) was used to quantify the pore-size distribution as shown in Figure S1a. The average pore-body diameter and pore-throat width are 33 and 14 μm, respectively. More details of the pore-size distribution can be obtained from Chang et al. (2016). The same pore network was first used by Zuo et al. (2013) in their experiments on exsolution of dissolved CO_2, and has been used experimentally (Li et al., 2017) and numerically (Chen et al., 2018; Fakhari et al., 2018) in recent years. Micromodels #2 and #3 are two homogeneous and anisotropic micromodels, sharing the same elliptical silicon posts with different spacing, resulting in different longitudinal (k_l) and transverse (k_t) permeability. As shown in Figure 1, the throat width ratio between transverse and longitudinal is 0.50 in Micromodel #2 (II:I in Figure 1 for Micromodel #2) and 13.87 in Micromodel #3 (III:I in Figure 1 for Micromodel #3). The ratio of transverse permeability to longitudinal permeability (k_t/k_l) is calculated to be 0.63 in Micromodel #2 and 6.86 in Micromodel #3, using $k = \frac{1}{2}\left(\frac{A}{p}\right)^2$, where A and p represent the area and perimeter of the rectangular cross-section for fluid flow, respectively (White, 1979). More detailed calculation on the equation can be seen in the supporting information. Micromodel #4 is a homogeneous and isotropic hexagonal micromodel, with circular pore bodies connected to six pore throats. Figure S1b of the supporting information presents an example of the micromodel design including the pore network (#1) and the boundary conditions (Zuo et al., 2013). The triangle sections on each side of the pore allow for a uniform $scCO_2$ displacement before entering the pore network (see Figure S1c).

2.2 Experiments and imaging

An experimental setup with four high-pressure syringe pumps (Teledyne ISCO Inc., Lincoln, NE) was used for $scCO_2$ injection (ISCO 100 DM), water injection (ISCO 100 DM), back pressure control (ISCO 100 DM) and overburden pressure control (ISCO 500 DM). The schematic of the experimental setup can be seen in Figure S2 of the supporting information. Before a drainage experiment, a selected micromodel was cleaned by flowing through the following sequence of fluids: (1) deionized (DI) water, (2) isopropanol, (3) DI water, (4) SC-1 solution (DI water: NH_4OH: H_2O_2 at 5:1:1) and (5) DI water. The micromodel was then saturated with DI water. CO_2 and water were allowed to equilibrate to 40 °C for over 12 hours. After the above preparation steps, Coumarin -dyed $scCO_2$ was injected into the micromodel at a constant flow rate for each drainage experiment (Biswas et al., 1999). This sequence was repeated for a wide range of flow rates. Detailed descriptions of the experimental procedures can be found in Chang et al. (2017). Because $scCO_2$ was continuously injected into the micromodel, the dissolution of $scCO_2$ in residual water during drainage may have negligible effects on CO_2 saturation and distribution in the pore network. Under the experimental conditions (40 °C, 9 MPa), the solubility of $scCO_2$ dissolved in water is 1.225 mol/L (Spycher and Pruess, 2005). Meanwhile, in previous studies (Chang et al., 2016, 2017, 2019), we have showed the dissolution and mass transfer of $scCO_2$ in water in the sandstone-analogue Micromodel #1 is non-equilibrium, considerably limited by small area-to-volume ratios that represent the pore-throat configurations and characteristics of phase interfaces.

Table 2 lists the imposed volumetric injection rates for the four micromodels. The displaced water during drainage was collected in a syringe pump that was used to maintain pressure. These rates correspond to a range of Darcy velocity from 1.23 m/day to 2,775 m/day, and a range of $logC_a$ from -7.60 to -4.41. The classic capillary number was calculated using an equation with contact angle considered by Lenormand et al. (1988) defined by

$$C_a = (\mu \times \overline{u})/(\sigma \times cos\theta), \quad (1)$$

where θ is the contact angle between the injected and resident fluid. The contact angle of $scCO_2$ and water on the silica surface is measured as 15.2°±0.4° (Table 1 and Figure S3 in the Supporting Information), similar to Wang et al. (2012) using the same silicon wafers and fluorescent dye for $scCO_2$. The other parameters are the same as in the original form given by Saffman and Taylor (1958).

The imposed range of injection rates correspond to flow rates at 0.03 to 50 m away from an injection well (with an injection rate of one million metric tonnes of $scCO_2$ per year over a screen length of 15 m with uniform flow assumed) at a typical geological CO_2 sequestration (GCS) site. During each drainage experiment, $scCO_2$ was injected into the micromodel at a specified constant flow rate until the quasi-steady state was reached, i.e., $scCO_2$ distribution and saturation remained stable with time. The experiment was then stopped, and the micromodel was thoroughly cleaned and saturated with water before the next experiment was conducted at a different rate. An additional experiment was conducted in the sandstone-analog micromodel (#1) using step-rate $scCO_2$ injection, i.e., the injection rate was increased after the quasi-steady-state conditions were reached for a given rate. This represents an alternative injection approach that was explored to increase $scCO_2$ storage capacity (White et al., 2014).

The stained scCO_2 in the micromodel was observed through a Blue GFP filter set (λ_{ex} = 379-401 nm, λ_{em} = 435-485 nm). The micromodel images were acquired using a Nikon Eclipse TE2000-E epifluorescent microscope (Melville, NY) through a 4X inverted objective with a spatial resolution of 1.62 μm/pixel. A single image that captured the entire pore network was formed by montaging multiple separate sub-images taken by a CoolSnap HQ2 monochrome CCD camera (Photometrics Inc., Tucson, AZ). The camera was controlled by a computer with imaging software (NIS-Elements, Nikon, Melville, NY).

The fluorescent signal intensity of dyed scCO_2 is significantly higher than that for silicon posts and pore spaces filled with water, with a signal-to-noise ratio >10. A threshold value can be unambiguously determined for each image to distinguish scCO_2 phase from others. During scCO_2 drainage, time-lapse images were obtained until the quasi-steady state was reached, i.e., the intensity of the dyed scCO_2, and the scCO_2 distribution and saturation kept constant with time. To better observe the scCO_2-water distribution in (heterogeneous) Micromodel #1, images of the dyed scCO_2 and the pore space were overlapped. Segmentation and analysis of these images were conducted by using ImageJ software (Rasband, 1997-2019). We validated the image segmentation method and fabrication process by comparing (1) the measured porosity from fluorescent images and the computed one from the micromodel design and (2) the measured size of the silicon posts and the design value. Both comparisons showed good agreement with errors <5%. For Micromodel #3, images taken at a resolution of 1.62 μm/pixel failed to capture the pore throat with 3 µm width (see Figure 1). This leads to an error in image segmentation and underestimate pore volume by <2.5% of design.

3. Results and Discussion

3.1 Effects of pore characteristics on drainage fingering and $scCO_2$ saturation

Figures 2-5 show the fluorescent images of $scCO_2$ distribution after quasi-steady state was reached in the four micromodels. The numbers in the parentheses are the $logC_a$ values and corresponding $scCO_2$ saturations. The different $scCO_2$ saturations and distributions in the four micromodels under similar experimental conditions indicate the effects of pore characteristics on drainage.

In Micromodel #1, three displacement patterns with varying $scCO_2$ injection rates can be observed (see Figure 2). At low injection rates ($logC_a$ < −6.59), the drainage process is dominated by a high capillary force. As a result, $scCO_2$ invades simultaneously into high-permeability channels and their neighboring pores/throats through randomly distributed forward and lateral flow paths, leaving clusters of entrapped water. Such a displacement pattern can be attributed to capillary fingering (Zhang et al., 2011b; Wang et al., 2012). At the lowest displacement rate ($logC_a$=−7.29), the CO_2 saturation and distribution remained constant with time after 35 PVs (4.7 hours) of $scCO_2$ injection. At quasi-steady state, pores/pore clusters filled with $scCO_2$ are isolated by water in the pore throats, i.e., $scCO_2$ snap-off during drainage occurs (marked by the white arrows and shown by the magnified image) under the high capillary force when a low $scCO_2$ injection rate is used. Correspondingly, $scCO_2$ saturation (S_{CO2}) decreases slightly from 0.48 at $logC_a$=

-7.29 to 0.41 at $logC_a = -6.99$.

At higher injection rates ($logC_a > -6.29$), $scCO_2$ enters the high-permeability channels and their neighboring pores/pore throats simultaneously in continuous flow paths and plumes, with a great reduction in entrapped water clusters. Snap-off and $scCO_2$-water redistribution are not observed. The displacement is dominated by viscous fingering. S_{CO2} increases considerably from 0.54 at $logC_a = -5.59$ to 0.88 at $logC_a = -4.41$, as $scCO_2$ is able to invade additional small pores/pore throats due to the higher viscous force. At intermediate injection rates ($logC_a = -6.59$ and -6.29), crossover from capillary to viscous fingering is observed: low-viscosity $scCO_2$ preferentially flows along the high-permeability channels by invading the interior pores/pore throats and bypasses the majority resident water outside. Meanwhile, a couple of lateral $scCO_2$ flow paths develop at locations marked by yellow arrows, indicating the co-existing capillary and viscous fingering. The lateral CO_2 fingers have been observed through numerical simulations with reduced capillary numbers (Chen et al., 2018). A decrease in S_{CO2} occurs in the crossover zone, from 0.41 at $logC_a = -6.99$ to 0.35 at $logC_a = -6.59$ and 0.37 at $logC_a = -6.29$, similar to the observations from Wang et al. (2012) and Lenormand et al. (1988).

Drainage fingering and crossover with varying injection rates in Micromodel #2 with low anisotropy are shown in Figure 3. The drainage pattern in this pore network is characterized by a main continuous zone (marked by the white dotted lines) near the upstream end with several narrow $scCO_2$ flow paths (1-3 pore bodies in width) stretching out towards the outlet. The main plume fronts keep consistent over time after drainage. The boundary of the main plume and the branching flow paths, however, varies with $scCO_2$ injection rates and the dominant force. At lower injection rates ($logC_a$< −6.20), the capillary force dominates the displacement, resulting in snap-off of branching flow paths (marked by white arrows) and an irregular plume boundary. At higher injection rates ($logC_a$> −6.20), the main plume with smooth boundary invades further into the pore network, and additional flow paths develop continuously stretching out to the outlet. At the maximum injection rate with $logC_a$= −4.72, the $scCO_2$ migrates throughout the pore network without clear boundaries between the continuous zone and branches, indicating that the viscous force controls the displacement. At an intermediate injection rate ($logC_a$= −6.20), flow occurs primarily in a few pathways in the middle of the pore network, indicating a reduction in displacement efficiency. Only two $scCO_2$ flow paths develop and stretch out to the outlet, bypassing large water-saturated regions even after >1100 pore volumes (PV) of $scCO_2$ are injected. S_{CO2} is 0.24 and 0.20 at $logC_a$= −6.90 and $logC_a$= −6.60, respectively, followed by a large decrease at the crossover zone ($logC_a$= −6.20) to 0.08. S_{CO2} finally increases to ~0.35 at larger injection rates ($logC_a$> −6.20).

In Micromodel #3, displacement is dominated by large transverse permeability ratio of the pore network (k_t/k_l=6.86). As shown in Figure 4, $scCO_2$ widely invades the entire pore network at lower injection rates ($logC_a$= −6.31 and −5.61), leaving some small water clusters near the inlet. At higher injection rates, $scCO_2$ thoroughly invades these water clusters, increasing $scCO_2$ saturation from 0.88 at $logC_a$= −6.31 to 0.93 at $logC_a$= −4.43. Compared to the previous two micromodels, S_{CO2} in

Micromodel #3 shows the highest value under the similar range of drainage flow rates imposed.

Displacement in Micromodel #4 shows very different drainage characteristics. As can be seen in Figure 5, at $logC_a$= −7.60, $scCO_2$ invades the pore network in three narrow flow paths. More flow paths develop with increasing displacement rates. At $logC_a$= −4.72, $scCO_2$ invades over 80% of the pore space with small entrapped water bodies. In contrast to the observations in Micromodels #1 and #2, no crossover zone develops as S_{CO2} monotonically increases with injection rate. This monotonic relation between non-wetting phase saturation and capillary number was also observed by Zhang et al. (2011b) using fluid pairs with viscosity ratio of $logM$= −1.34, but with C_a values that are two orders of magnitude higher. They claimed that the observed displacement pattern could be characterized as viscous fingering, except for the displacement patterns at their lowest C_a ($\log C_a = -5.26$) in the crossover zone. The displacement in Micromodel #4 in this study, with two orders of magnitude smaller C_a, shows a similar viscous-force dominance. More detailed discussion can be seen in Section 3.2.

3.2 A complete capillary scaling with pore characteristics

The relationship between $logC_a$ and $scCO_2$ saturation for all drainage experiments conducted for each of the four micromodels is shown in Figure 6a. In addition to the results obtained in this study, data from Zhang et al. (2011b) and Wang et al. (2012) are also shown in this figure, with estimated non-wetting fluid saturations from their published figures. Under the similar conditions of 9.0 MPa and 41°C, Wang et al. (2012) conducted $scCO_2$ drainage tests in a homogeneous isotropic pore network (referred to as #C1) that consisted of cylindrical silicon posts 200 μm in diameter, 120 μm pore bodies, and 26.7 μm pore throats. At ambient conditions and using dodecane as the non-wetting fluid and polyethylene glycol 200 as the wetting fluid ($logM$= −1.34), Zhang et al. (2011b) investigated drainage mechanisms in a similar micromodel to that used by Wang et al. (2012) (referred to as #C2) that consisted of cylindrical silicon posts 300 μm in diameter, 180 μm pore bodies, and 40 μm pore throats. The fluid pairs used in their study have a similar viscosity ratio to $scCO_2$-water system. For Micromodels #1, #2 and #C1, crossover zones with large reductions in $scCO_2$ saturation are observed. For Micromodel #C2, the lowest flow rate ($logC_a$= −5.26) is characterized as the crossover zone by Zhang et al. (2011b), indicating that the full transition from capillary fingering is missed from their experiments. Figure 6a shows that $logC_a$ in the crossover zones for the four micromodels varies from −6.59 to −5.26. Meanwhile, monotonic increase in CO_2 saturation with $logC_a$ (without crossover) is observed for Micromodels #3 and #4 in which the minimum pore throats are less than 4 μm. In summary, the drainage fingering and crossover are significantly affected by pore characteristics that are not considered in the classic (dimensionless) capillary number.

Dullien (1992) claimed that the classic capillary number C_a does not deserve to be called a *measure* of the ratio of viscous-to-capillary forces for subsurface flow, as viscous forces are known to be proportional to a length scale L in the direction of flow, and capillary forces are proportional to a characteristic pore size. He then proposed a *complete capillary number* (C_a^*) to account for pore characteristics. Assuming a rectangular cross-section for fluid flow, the viscous force $\mathrm{F_v}$ is equal to the wall shear stress τ_w multiplied by the surface area of the flow path:

$$F_v = 2\tau_w(a+b)L, \tag{2}$$

where a and b refer to the pore-throat diameter and micromodel depth. Assuming viscous (Poiseuille) flow, the shear stress can be written as

$$\tau_w = 4\mu\bar{u}\left(\frac{1}{a}+\frac{1}{b}\right), \tag{3}$$

where $\bar{u}$ is the average velocity. Combining Eqs (2) and (3) leads to

$$F_v = 8\mu\bar{u}L(a+b)\left(\frac{1}{a}+\frac{1}{b}\right). \tag{4}$$

The capillary force F_c is equal to the capillary pressure P_c times the area of the rectangular cross section (i.e., ab). With the capillary pressure expressed as

$$P_c = 2\sigma cos\theta\left(\frac{1}{a}+\frac{1}{b}\right), \tag{5}$$

the capillary force can be written as

$$F_c = 2\sigma ab cos\theta\left(\frac{1}{a}+\frac{1}{b}\right) \tag{6}$$

Finally, the ratio of the viscous-to-capillary forces can be defined by the *complete capillary number*:

$$C_a^* = \frac{4\mu\bar{u}L}{\sigma cos\theta}\left(\frac{1}{a}+\frac{1}{b}\right) = 4C_aL\left(\frac{1}{a}+\frac{1}{b}\right) \tag{7}$$

It is clear from Eq. (7) that, theoretically, C_a is not sufficient to quantify the *true* ratio of viscous-to-capillary forces in porous media with different characteristic length (L), pore-throat diameter (a) and depth of the micromodel (b). The lack of geometric information in C_a may contribute to the differences in the observed $logC_a$-saturation relations.

We re-scaled the measurement data using the *complete capillary number* in Eq. (7). For the homogeneous pore networks (#2, #3, #4, #C1 and C#2), we assumed L equals the distance between two silicon post centers parallel to the flow direction, while a is the diameter of the pore throat in the isotropic pore networks (#4, #C1 and #C2) and the smallest diameter of pore throats in the anisotropic pore networks (#2 and #3), b=37 μm for #2, #3 and #4, 35 μm for #C1 and 53 μm for #C2. For (heterogeneous) Micromodel #1, L is the characteristic length of ~580 μm along the flow direction (marked by the white lines in Figure S4) for all pore/scCO_2 clusters and a=14.0 μm, b = 35 μm for the average diameter of pore throat and depth of the micromodel, respectively. The pore network of Micromodel #1 resembles a repetitive structure at ~580 μm in length, in which large pore clusters are connected by narrow pore throats (see Figure S4a), resulting in large scCO_2-invaded clusters connected by constrictive narrow flow paths after drainage (see Figure S4b). Table 2 lists the values of C_a^* and the involved parameters for calculating C_a^* for the micromodels considered in Figure 6.

The revisited relationships between $logC_a{}^*$- non-wetting fluid saturation are shown in Figure 6b. The re-scaled crossover zones for Micromodels #1, #2 and #C1 share the similar minimum value at $logC_a^* = -4.0$. The crossover zone minimum for Micromodel #C2 (at the lowest injection rate) is at $logC_a^* = -3.48$, because the full crossover zone was not available from the experimental data. The disparate crossover zones presented as a function of C_a in Figure 6a are re-scaled by using C_a^* to have a unified crossover zone, no matter what specific pore-scale characteristics are involved.

It is shown that the complete capillary number with consideration of pore characteristics can better quantify the drainage fingering and crossover regimes in different pore networks than the classic capillary number. This is the first time to quantify the unstable drainage in different pore networks using the complete capillary number.

The complete capillary number was used in a few studies to quantify displacement characteristics in single pore networks. Dong et al. (1998) characterized the saturation-profile histories of water imbibition in sand packs using C_a^*. Nobakht et al. (2007) quantified their experiments on CO_2-EOR in a sand pack and showed an increase in oil recovery for $logC_a^* > -3.20$. Their higher C_a^* value at the saturation minimum of non-wetting phase fluid may be attributed to the longer characteristic length in a larger three-dimensional media.

The crossover zone was not observed in the experiments conducted in Micromodel #4 as $scCO_2$ saturation increased monotonically with $logC_a^*$. As shown in Figure 5, the $scCO_2$ distribution in Micromodel #4 indicates the viscous force dominates pore-filling displacement, which may be attributed to the significant interfacial dynamics at the $scCO_2$-water interface by the small pore throat and high pore-throat ratio (12:1). These dynamics have been discussed in the literature for drainage experiments in pore networks with high pore-throat ratios. Armstrong et al. (2013) used a micromodel with similar pore characteristics, i.e., 60 µm spherical pore bodies connected to six 13 µm pore throats (with a pore-throat aspect ratio at 4.6), conducted drainage experiments for a decane-water system, and observed the rapid interfacial dynamics, e.g., interfacial velocities and capillary pressure gradients at the millisecond scale. They concluded that (1) the interfacial velocities (displacement velocities of a meniscus at the immiscible interface) can be six times higher than the mean front velocity (Darcy velocity) during Haines jumps, and (2) the displacement characteristics at the pore-network scale greatly depend on the dynamic, interfacial displacement at the local pore scale (<10 pores). The Haines jump shows a sudden increase in the interfacial velocity and a drop in the capillary pressure when the non-wetting phase passes from a pore neck into a wider pore body, displacing the wetting phase (Haines, 1930). Moebius and Or (2012) observed the Haines jump events at millisecond resolution in sinusoidal capillaries (pore-throat ratio at 4.0), and found that the interfacial velocities during a Haines jump exceeded 50 times mean front velocity. Modeling results also indicated that the interfacial velocities exponentially increase with the pore-throat ratio, imposing a more significant effect on the phase distribution in the entire pore network. Note that in Micromodel #4, the relatively high pore-throat ratio of 12:1 may yield high interfacial velocities at local pores/pore cluster scale, which result in the viscous drainage pattern and monotonic increase in S_{CO2} with $logC_a^*$ at the pore-network scale.

For Micromodel #3, the large permeability ratio (k_t/k_l=6.86) greatly enhances scCO_2 transverse flow and yields high displacement efficiency and scCO_2 saturations (>0.80) for all water-injection rates. By comparison, scCO_2 saturations in Micromodel #3 are higher than those in (isotropic cylindrical) Micromodel #C1, which, in turn, are higher than those observed in Micromodel #2 with a lower permeability ratio

(k_t/k_l=0.63), demonstrating the effect of anisotropy of porous media on drainage efficiency and $scCO_2$ saturation.

3.3 Constant-rate vs. step-rate injection

In addition to the transition from capillary to viscous fingering, it is also of interest to investigate the effect of capillary fingering on viscous fingering in a single experiment. We conducted a step-rate $scCO_2$ injection experiment in the sandstone-analog micromodel (#1) to investigate (1) an alternative injection approach that can be explored to increase $scCO_2$ saturation (Wang et al., 2012; White et al., 2014), and (2) the dynamic CO_2 invasion in a heterogeneous porous media with increasing capillary number. As shown in Figure 7a, the initially water-saturated micromodel is first flooded by $scCO_2$ injection at 50 μL/h ($logC_a$= −6.59) until a quasi-steady state with stable CO_2 saturation of 0.35 is reached after 270 min and 167 PV injected $scCO_2$. The $scCO_2$ injection rate is then increased to 2,500 μL/h ($logC_a$= −4.89) and maintained for 420 min (4,800 PV $scCO_2$ injected) until CO_2 saturation is stable at 0.58. Finally, CO_2 injection rate is increased to 7,500 μL/h ($logC_a$= −4.41). At the end of the experiment (530 min, over 14,000 PV $scCO_2$ injected), CO_2 saturation remains stable at 0.75. Within the first 1 min of each rate increase, CO_2 saturation increases sharply. At the same displacement rates of $logC_a$= −4.89 and −4.41 and by the constant-rate injection approach, smaller $scCO_2$ injection volumes are needed at 1852 and 5556 PVs, respectively, to reach a higher quasi-steady state CO_2 saturations of 0.81 and 0.88.

To better understand the dynamic CO_2 invasion, we visualize in Figure 7b the newly developed CO_2 distribution (marked by different colors) at the end of each step injection rate with slow S_{CO2} increase and at the end of sharp S_{CO2} change 1 min after each step-rate increase. The corresponding $scCO_2$ injection volume and saturation at the five nodes are shown by red squares in Figure 7a. As shown in Figure 7b, displacement of water occurs first from the three channels with large pores under the lowest injection rate ($logC_a$= −6.59). As injection rate increases, water in smaller pores next to the channels is displaced by a higher viscous force. However, water from the relatively small pores/pore throats is displaced very slowly. This fast displacement followed by a slow displacement occurs for each step injection rate. Eventually, only 25% of the initial water remains in the heterogeneous micromodel, including the contributions from the capillary end effect near the downstream under the extremely high injection rate.

By comparison, the step-rate injection method is not as efficient as the constant-rate injection method, because the quasi-steady-state CO_2 saturation at each step of the step-rate injection is smaller than that for the corresponding constant-rate injection (see Figure 7c), and more pore volumes of $scCO_2$ injection are required to reach the quasi-steady state. The reduced efficiency of displacement depends on the CO_2 distribution after the first step of the step-rate injection test. In our case, the first step of the test creates flow channels with lowest S_{CO2} at the crossover zone ($logC_a$= −6.59) (also see Figure 2). As shown in the insert of Figure 7c, Wang et al. (Wang et al., 2012) started the step-rate injection from a higher S_{CO2} at the capillary fingering regime with $logC_a = -7.61$, leading to an increased efficiency of displacement in comparison with the constant-rate injection method. These different observations imply the role of initial phase distribution on CO_2 distribution and saturation during the step-rate injection, though capillary end effect exists in both studies. When the step-rate injection method is used, it is important to initiate the process from the capillary fingering regime for enhanced displacement efficiency.

4. Conclusions

The impacts of pore geometry and pore-network topology on scCO_2-water drainage fingering have been investigated using displacement experiments in four micromodels. These micromodels represent pore networks with varying anisotropy and heterogeneity. For each experiment, high-resolution images of scCO_2-water distributions were obtained (from which scCO_2 saturation was derived) using a fluorescence imaging system.

The scCO_2 distributions and saturations at quasi-steady state show the entire spectrum of scCO_2 drainage, from capillary fingering through crossover to viscous fingering, with increase in $logC_a$ for the homogeneous and low-anisotropy elliptical micromodel (#2) and the heterogeneous sandstone-analog micromodel (#1). For both micromodels, a large reduction in scCO_2 saturation was observed in the crossover zone, although the corresponding $logC_a$ ranges are different. The disparate crossover zones with $logC_a$ was attributed to the absence of pore characteristics in the classic capillary number. Re-scaling using the complete capillary number with pore characteristics considered led to similar scCO_2 saturation minima at $logC_a^* = -4.0$. A monotonic increase in $scCO_2$ saturation and drainage efficiency with capillary number and no crossover were observed for the isotropic hexagonal network (#4) and the high-anisotropy elliptical micromodel (#3). These observations indicate that there are large impacts of pore geometry and pore-network topology on unstable drainage fingering and that the complete capillary number can be used for improved comparisons between different micromodels. The measured CO_2 saturations in these centimeter-scale micromodels vary considerably from 0.08 to 0.93 depending on the pore characteristics and displacement rates.

Our experimental observations indicate that the impacts of pore geometry and pore-network topology on unstable drainage fingering are significant and the complete capillary number can be used to improve the characterization of flow regimes in different micromodels. Results from this study may deepen our understanding in the fundamentals of pore-scale displacement and impacts from porous media for GCS. Specially, the re-scaled relationship between $logC_a^*$ and S_{CO2} may have implications for a field-scale GCS project. With the increase in the distance from an injection well, the drainage velocity and thus viscous force decrease, and the displacement regime may change from dominant viscosity fingering to dominant capillary fingering, with or without crossover that depends on the pore structures of the storage formation. All the drainage tests in this study were conducted in strongly water-wet micromodels. The wettability of the solid surface will inevitably affects the $scCO_2$ fingering flow pattern and saturation. Some recent studies, e.g., Zhao et al. (2016) and Hu et al. (2017, 2018) have showed a wider $scCO_2$ fingering front and more compact displacement patterns with increasing the displacement efficiency in micromodels more affinitive to the displacing fluid. The effects of wettability on $scCO_2$ fingering regimes and crossover, however, need further experimental investigations with a broader range of displacement rates. It is also noted that gravity was not considered in the 2-D pore networks for all drainage experiments in this study. In the field, the viscous/capillary $scCO_2$ fingers may coincidence with high-permeability channels (Birkholzer et al., 2015), while local pore structures and small fingers may become secondary in affecting $scCO_2$ plume. The non-uniform displacement and channeling flow of $scCO_2$ (e.g., in Micromodel #2) may cause local pressure buildup, increase leakage potential through caprock and limit the storage capacity (Zhou and Birkholzer, 2011; Abdullah et al., 2013). In addition, the interplay between viscous/capillary fingering and gravity is also important because the latter is dominant in shaping 3-D plume as shown by both analytical (Nordbotten et al., 2005) and numerical (Zhou et al., 2008; Zhou and Birkholzer, 2011) modeling, as well as laboratory experiments (Cinar et al., 2009; Rostami et al., 2010; Suekane et al., 2015; Trevisan et al., 2014, 2015, 2017).

Supporting information

More detailed information and images on the experimental setup and pore-size characterization are provided in the Supporting information.

Notes

The authors declare no competing financial interest.

Acknowledgements

This material was based upon the work supported by the U.S. Department of Energy, Office of Science, Office of Basic Energy Sciences, Energy Frontier Research Centers program under Contract No. DE-AC02-05CH11231. The first author was also supported by the National Natural Sciences Foundation of China (Grant No. 51704297), China Postdoctoral Science Foundation (Grant No. 2016M601173) and the State Key Research Development Program of China (Grant No. 2016YFC0600705). The micromodel experiments were conducted at the William R. Wiley Environmental Molecular Sciences Laboratory (EMSL), a scientific user facility of the U.S. Department of Energy's Office of Biological and Environmental Research operated by the Pacific Northwest National Laboratory (PNNL).

References

Abdullah, C., Birkholzer, J.T., Zhou, Q., 2013. Pressure buildup and brine migration during CO_2 storage in multilayered aquifers. Ground Water 51 (2), 252–267.

Akbarabadi, M., Piri, M., 2013. Relative permeability hysteresis and capillary trapping characteristics of supercritical CO_2/brine systems: an experimental study at reservoir conditions. Adv. Water Resour. 52, 190–206.

Armstrong, R.T., Steffen, B., 2013. Interfacial velocities and capillary pressure gradients during Haines jumps. Phys. Rev. E 88 (4), 600–614.

Armstrong, R.T., Georgiadis, A., Ott, H., Klemin, D., Berg, S., 2014. Critical capillary number: Desaturation studied with fast X-ray computed microtomography. Geophys. Res. Lett. 41, 55–60, doi:10.1002/2013GL058075.

Bachu, S., 2013. Drainage and imbibition CO2/brine relative permeability curves at in situ conditions for sandstone formations in western Canada. Energy Proc. 37, 4428–4436.

Bachu, S., 2015. Review of CO_2 storage efficiency in deep saline aquifers. Int. J. Greenhouse Gas Control 40, 188–202.

Bandara, U.C., Oostrom, M., Tartakovsky, A.M., Palmer, B.J., Zhang, C., Grate, J.W., 2013. Comparison of pore-scale numerical simulations of unstable immiscible displacements in porous media with micromodel experiments. Adv. Water Resour. 62, 356–369.

Bennion, D.B., Bachu, S., 2008. Drainage and imbibition relative permeability relationships for supercritical CO_2/brine and H_2S/brine systems in intergranular sandstone, carbonate, shale, and anhydrite rocks. SPE Reserv. Eval. Eng., 11 (3), 487–496.

Bennion, D.B., Bachu, S., 2010. Drainage and imbibition CO2/brine relative per-meability curves at reservoir conditions for carbonate formations, SPE Paper134028.

Berg, S., Ott, H., 2012. Stability of CO_2–brine immiscible displacement. Int. J. Greenhouse Gas Control 11, 188–203.

Birkholzer, J.T., Oldenburg, C.M., Zhou, Q., 2015. CO_2 migration and pressure evolution in deep saline aquifers. Int. J. Greenhouse Gas Control 40, 203–220.

Biswas, R., Lewis, J.E., Maroncelli, M., 1999. Electronic spectral shifts, reorganization energies, and local density augmentation of coumarin 153 in supercritical solvents. Chem. Phys. Lett. 310 (5-6), 485−494.

Chang, C., Zhou, Q., Xia, L., Li, X., Yu, Q., 2013. Dynamic displacement and non-equilibrium dissolution of supercritical CO_2 in low-permeability sandstone: An experimental study. Int. J. Greenhouse Gas Control 14, 1–14.

Chang, C., Zhou, Q., Guo, J., Yu, Q., 2014. Supercritical CO_2 dissolution and mass transfer in low-permeability sandstone: Effect of concentration difference in water-flood experiments. Int. J. Greenhouse Gas Control 28, 328–342.

Chang, C., Zhou, Q., Kneafsey, T. J., Oostrom, M., Wietsma, T.M., Yu, Q., 2016. Pore-scale supercritical CO_2 dissolution and mass transfer under imbibition conditions. Adv. Water Resour. 92, 142–158.

Chang, C., Zhou, Q., Oostrom, M., Kneafsey, T.J., Mehta, H., 2017. Pore-scale supercritical CO_2 dissolution and mass transfer under drainage conditions. Adv. Water Resour. 100, 14–25.

Chang, C., Zhou, Q., Kneafsey, T.J., Oostrom, M., Ju, Y., 2019. Coupled supercritical CO_2 dissolution and water flow in pore-scale micromodels. Adv. Water Resour. 123, 54–69.

Chen, Y., Li, Y., Valocchi, A.J., Christensen, K.T., 2018. Lattice Boltzmann simulations of liquid CO_2 displacing water in a 2D heterogeneous micromodel at reservoir pressure conditions. J. Contam. Hydrol. 212, 14–27.

Chomsurin, C., Werth, C.J., 2003. Analysis of pore-scale nonaqueous phase liquid dissolution in etched silicon pore networks. Water Resour. Res. 39 (9), 1265, doi:10.1029/2002WR001643.

Cinar, Y., Riaz, A., Tchelepi, H.A., 2009. Experimental study of CO_2 injection into saline formations. SPE J. 4 (4), 588–594.

Cottin, C., Bodiguel, H., Colin, A., 2010. Drainage in two-dimensional porous media: from capillary fingering to viscous flow. Phys. Rev. E 82 (4), 046315.

DeHoff, K.J., Oostrom, M., Zhang, C., Grate, J.W., 2012. Evaluation of two-phase relative permeability and capillary pressure relations for unstable displacements in a pore network, Vadose Zone J. 11 (4), doi:10.2136/vzj2012.0024.

Dong, M., Dullien, F.L., Zhou, J., 1998. Characterization of waterflood saturation profile histories by the ‘complete’ capillary number. Transp. Porous Med. 31, 213–237.

Dullien, F.A.L., 1992. Porous Media: Fluid Transport and Porous Structure.

Academic Press, SanDiego, CA.

Fakhari, A., Li, Y., Bolster, D., Christensen, K.T., 2018. A phase-field lattice Boltzmann model for simulating multiphase flows in porous media: Application and comparison to experiments of CO_2 sequestration at pore scale. Adv. Water Resour. 114, 119–134.

Ferer, M., Ji, C., Bromhal, G.S., Cook, J., Ahmadi, G., Smith, D.H., 2004. Crossover from capillary fingering to viscous fingering for immiscible unstable flow: Experiment and modeling. Phys. Rev. E 70 (1), 016303.

Ferer, M., Brohmal, G.S., Smith, D.H., 2005. Two phase flow in porous media: crossover from capillary fingering to compact invasion for drainage. Phys. Rev. E 71, 026303.

Ferer, M., Bromhal, G.S., Smith, D.H., 2007. Crossover from capillary fingering to compact invasion for two-phase drainage with stable viscosity ratios. Adv. Water Resour. 30 (2), 284–299.

Ferer, M., Anna, S.L., Tortora, P., Kadambi, J.R., Oliver, M., Bromhal, G.S., Smith, D.H., 2011. Two-phase flow in porous media: predicting its dependence on capillary number and viscosity ratio. Transp. Porous Med. 86 (1), 243–259.

Haines, W.B., 1930. Studies in the physical properties of soil. V. The hysteresis effect in capillary properties, and the modes of moisture distribution associated therewith. J. Agric. Sci. 20 (01), 97–116.

Hildebrand, T., Rüesgsegger, P., 1996. A new method for the model-independent assessment of thickness in three-dimensional images. J of Microscopy 185, 67–75.

Hu, R., Wan, J., Kim, Y., Tokunaga, T.K., 2017. Wettability effects on supercritical CO_2–brine immiscible displacement during drainage: Pore-scale observation and 3D simulation. Int. J. Greenhouse Gas Control 60, 129–139.

Hu, R., Wan, J., Yang, Z., Chen, Y., Tokunaga, T.K., 2018. Wettability and flow rate impacts on immiscible displacement: A theoretical model. Geophys. Res. Lett. 45, 3077–3086.

IPCC, 2005. Special report on carbon dioxide capture and storage. In: Metz, B., Davidson, O., de Coninck, H.C., Loos, M., Meyer, L.A. (Eds.). Prepared by Working Group III of the Intergovernmental Panel on Climate Change. Cambridge University Press, Cambridge, United Kingdom and New York, NY, USA.

Krevor, S.C.M., Pini, R., Zuo, L., Benson, S.M., 2012. Relative permeability and trapping of CO_2 and water in sandstone rocks at reservoir conditions. Water Resour. Res. 48, W02532, http://dx.doi.org/10.1029/2011WR010859.

Lenormand, R., Touboul, E., Zarcone, C., 1988. Numerical models and experiments on immiscible displacements in porous media. J. Fluid Mech. 189, 165–187.

Li, Y., Kazemifar, F., Blois, G., Christensen, K.T., 2017. Micro-PIV measurements of multiphase flow of water and liquid CO_2 in 2D heterogeneous porous micromodels. Water Resour. Res. 53, 6178–6196.

Moebius, F., Or, D., 2012. Interfacial jumps and pressure bursts during fluid displacement in interacting irregular capillaries. J. Colloid Interface Sci. 377 (1), 406–415.

Nobakht, M., Moghadam, S., Gu, Y., 2007. Effects of viscous and capillary forces on CO_2 enhanced oil recovery under reservoir conditions. Energ. Fuel 21 (6), 3469–3476.

Nordbotten, J.M., Celia, M.A., Bachu, S., 2005. Injection and storage of CO_2 in deep saline aquifers: analytical solution for CO_2 plume evolution during injection. Transp. Porous Med. 58 (3), 339–360.

Pini, R., Krevor, S.C.M., Benson, S., 2012. Capillary pressure and heterogeneity for the CO_2/water system in sandstone rocks at reservoir conditions. Adv. Water Resour. 38, 48–59.

Rasband, W.S., 1997-2019. ImageJ, U.S.,National Institutes of Health, Bethesda, Maryland, USA, https://imagej.nih.gov/ij/.

Rostami, B., Kharrat, R., Pooladi-Darvish, M., Ghotbi, C., 2010. Identification of fluid dynamics in forced gravity drainage using dimensionless groups. Transp. Porous Med. 83, 725–740.

Saffman, P.G., Taylor, G., 1958. The penetration of a fluid into a porous medium or Hele-Shaw cell containing a more viscous liquid. Proc. R. Soc. A 245, 312–329.

Senel, O., Will, R., Butsch, R.J., 2014. Integrated reservoir modeling at the Illinois Basin – Decatur Project. Greenhouse Gases: Sci. Technol. 4 (5), 662–684.

Spycher, N., Pruess, K., 2005. CO_2–H_2O mixtures in the geological sequestration of CO_2. II. Partitioning in chloride brines at 12–100 °C and up to 600 bar. Geochim. Cosmochim. Acta 69 (13), 3309–3320.

Suekane, T., Saito, Y., Jiang, L., 2015. Non-wetting phase saturation after drainage from the wetting-phase-filled porous medium. J. Fluid Sci. Tech. 10 (2), DOI: 10.1299/jfst.2015jfst0014.

Toussaint, R., Måløy, K.J., Méheust, Y., Løvoll, G., Jankov, M., Schäfer, G., Schmittbuhl, J., 2012. Two-phase flow: structure, upscaling, and consequences for macroscopic transport properties. Vadose Zone J. 11 (3), doi:10.2136/vzj2011.0123.

Tsuji, T., Jiang, F., Christensen K.T., 2016. Characterization of immiscible fluid displacement processes with various capillary numbers and viscosity ratios in 3D natural sandstone. Adv. Water Resour. 95, 3–15.

Trevisan, L., Cihan, A., Agartan, E., Mori, H., Fagerlund, F., Birkholzer, J.T., Zhou, Q., Illangasekare, T.H., 2014. Investigation of mechanisms of supercritical CO_2 trapping in deep saline reservoirs using surrogate fluids at ambient laboratory conditions. Int. J. Greenhouse Gas Control 29, 35–49.

Trevisan, L., Pini, R., Cihan, A., Birkholzer, J.T., Zhou, Q., Illangasekare, T.H., 2015. Experimental analysis of spatial correlation effects on capillary trapping of supercritical CO_2 at the intermediate laboratory scale in heterogeneous porous media. Water Resour. Res. 51, 8791–8805, doi:10.1002/2015WR017440.

Trevisan, L., Pini, R., Cihan, A., Birkholzer, J.T., Zhou, Q., Gonzalez-Nicolas, A., Illangasekare, T.H., 2017. Imaging and quantification of spreading and trapping of carbon dioxide in saline aquifers using meter-scale laboratory experiments. Water Resour. Res. 53 (1), 485–502, doi:10.1002/2016WR019749.

Wang, Y., Zhang, C., Wei, N., Oostrom, M., Wietsma, T.W., Li, X., Bonneville, A., 2012. Experimental study of crossover from capillary to viscous fingering for supercritical CO_2–water displacement in a homogeneous pore network. Environ. Sci. Technol. 47, 212–218.

White, F.M., 1979. Fluid Mechanics. New York: McGraw-Hill, Chapter 6, 341.

White, J.A., Chiaramonte, L., Ezzedine, S., Foxall, W., Hao, Y., Ramirez, A., McNab, W., 2014. Geomechanical behavior of the reservoir and caprock system at the In Salah CO_2 storage project. Proc. Natl. Acad. Sci. U.S.A. 111 (24), 8747–8752.

Wilkinson, 1986. Percolation effects in immiscible displacement. Phys. Rev. A 34 (2), 1380–1391.

Willingham, T.W., Werth, C.J., Valocchi, A.J., 2008. Evaluation of the effects of porous media structure on mixing-controlled reactions using pore-scale modeling and micromodel experiments. Environ. Sci. Technol. 42 (9), 3185–3193.

Xu, B., Yortsos, Y.C., Salin, D., 1998. Invasion percolation with viscous forces. Phys. Rev. E 57, 739–751.

Zhang, C., Oostrom, M., Grate, J.W., Wietsma, T.W., Warner, M.G., 2011a. Liquid CO_2 displacement of water in a dual-permeability pore network micromodel. Environ. Sci. Technol., 45 (17), 7581-7588.

Zhang, C., Oostrom, M., Wietsma, T.W., Grate, J.W., Warner, M.G., 2011b. Influence of Viscous and Capillary Forces on Immiscible Fluid Displacement: Pore-Scale Experimental Study in a Water-Wet Micromodel Demonstrating Viscous and Capillary Fingering. Energ. Fuel 25 (8), 3493–3505.

Zhao, B., MacMinn, C.W., Juanes, R., 2016. Wettability control on multiphase flow in patterned microfluidics. Proc. Natl. Acad. Sci. U.S.A. 113 (37), 10251–10256.

Zheng, X., Mahabadi, N., Yun, T.S., Jang, J., 2017. Effect of capillary and viscous force on CO_2 saturation and invasion pattern in the microfluidic chip. J. Geophys. Res. Solid Earth 122, 1634–1647, doi:10.1002/2016JB013908.

Zhou, Q., Birkholzer, J.T., Tsang, C.F., Rutqvist, J., 2008. A method for quick assessment of CO_2 storage capacity in closed and semi-closed saline aquifers. Int. J. Greenhouse Gas Control 2, 626–639.

Zhou, Q., Birkholzer, J.T., 2011. On scale and magnitude of pressure build-up induced by large-scale geologic storage of CO_2. Greenhouse Gases: Sci. Technol. 1 (1), 11–20.

Zuo, L., Zhang, C., Falta, R.W., Benson, S.M., 2013. Micromodel investigations of CO_2 exsolution from carbonated water in sedimentary rocks. Adv. Water Resour. 53, 188–197.

List of Figures

Figure 1. Pore characteristics of the four micromodels used in this study, with silicon posts in black and pore space in white. The blue arrow indicates the $scCO_2$ flow direction during drainage experiments. The red lines indicate the nine identical sub-images in a 3 × 3 array for Micromodel #1. The magnified images for Micromodels #2 and #3 are not to scale.

Figure 2. Image of $scCO_2$ distribution in Micromodel #1 at the quasi-steady state after each drainage experiment. Silicon posts are shown in blue, water in black and $scCO_2$ in purple to white. $scCO_2$ flow is from left to right. The numbers in the parenthesis indicate ($logC_a$, S_{CO2}). White arrows and the magnified image show the snap-off of displacing $scCO_2$ at localities. Yellow arrows indicate transverse $scCO_2$ flow. The pore characteristics of the micromodel were shown at the top.

Figure 3. Image of $scCO_2$ distribution in Micromodel #2 at the quasi-steady state after each drainage experiment. $scCO_2$ is shown in orange to yellow, posts and water are in black. $scCO_2$ flow is from left to right. White dotted lines mark the main plume front in the pore network, while white arrows show the snap-off of drained $scCO_2$ at localities. The pore characteristics of the micromodel were shown at the top.

Figure 4. Image of $scCO_2$ distribution in Micromodel #3 at the quasi-steady state after each drainage experiment. $scCO_2$ is shown in orange to yellow, posts and water are in black. The pore characteristics of the micromodel were shown at the top.

Figure 5. Image of $scCO_2$ distribution in Micromodel #4 at quasi-steady state after drainage. $scCO_2$ is shown in orange to yellow, posts and water are in black. $scCO_2$ flow is from left to right. The pore characteristics of the micromodel were shown at the top.

Figure 6. (a) Non-wetting fluid saturation vs. $logC_a$ for the drainage experiments conducted in the four micromodels and in Wang et al. (2012) and Zhang et al. (2011b) with similar $logM$. (b) Re-scaled non-wetting fluid saturation vs. $logC_a{}^*$ using the complete capillary number. The numbers in each parenthesis indicate minimum non-wetting fluid saturation and the corresponding $logC_a$ or $logC_a{}^*$ value.

Figure 7. (a) $scCO_2$ saturation vs. injection volume and (b) dynamic $scCO_2$ distribution at early time (1 min) after the increase in each step rate and under quasi-steady state during the step-rate injection experiment in Micromodel #1, and (c) comparison of $logC_a$ vs. $scCO_2$ saturation between the constant- and step-rate experiments. The insert shows previous results from Wang et al. (2012).

Table 1. Micromodel Properties

Micromodel	#1	#2	#3	#4
Length×Width (cm×cm)	0.71×0.53	1.2×1.2	1.2×1.2	1.2×1.2
Depth (μm)	35	37	37	37
Porosity	0.35	0.47	0.25	0.44
Permeability (m^2)	7.4×10^{-13}	2.9×10^{-11}	1.1×10^{-13}	6.3×10^{-13}

Table 2. Summary of the experimental conditions and dimensionless number values

Micromodel	**#1**	**#2**	**#3**	**#4**	[1]**#C1**	[2]**#C2**
Q range (μL/h)	10-7500	50-7500	100-7500	10-7500	10-7500	5-7500
$\bar{u}$ range (m/d)	3.70-2775	5.75-862.5	22-1650	1.23-922.5	0.57- 425.03	0.39-580.55
θ	15.2°±0.4°					
$logM$	[1]-1.25					[2]-1.34
$logC_a$ range	−7.29-−4.41	−6.90-−4.72	−6.31-−4.43	−7.60-−4.72	−7.61-−4.73	−5.26-−2.08
L (μm)	580	413	403	90	226	340
a (μm)	14.0	13.0	3.0	5.0	26.0	40.0
b (μm)	35.0	37.0	37.0	37.0	35.0	53.0
$logC_a^*$ range	−4.76-−1.88	−4.49-−2.31	−3.28-−1.40	−5.44-−2.56	−5.76-−2.89	−3.43-−0.25

[1]Wang et al. (2012) and [2]Zhang et al. (2011b).

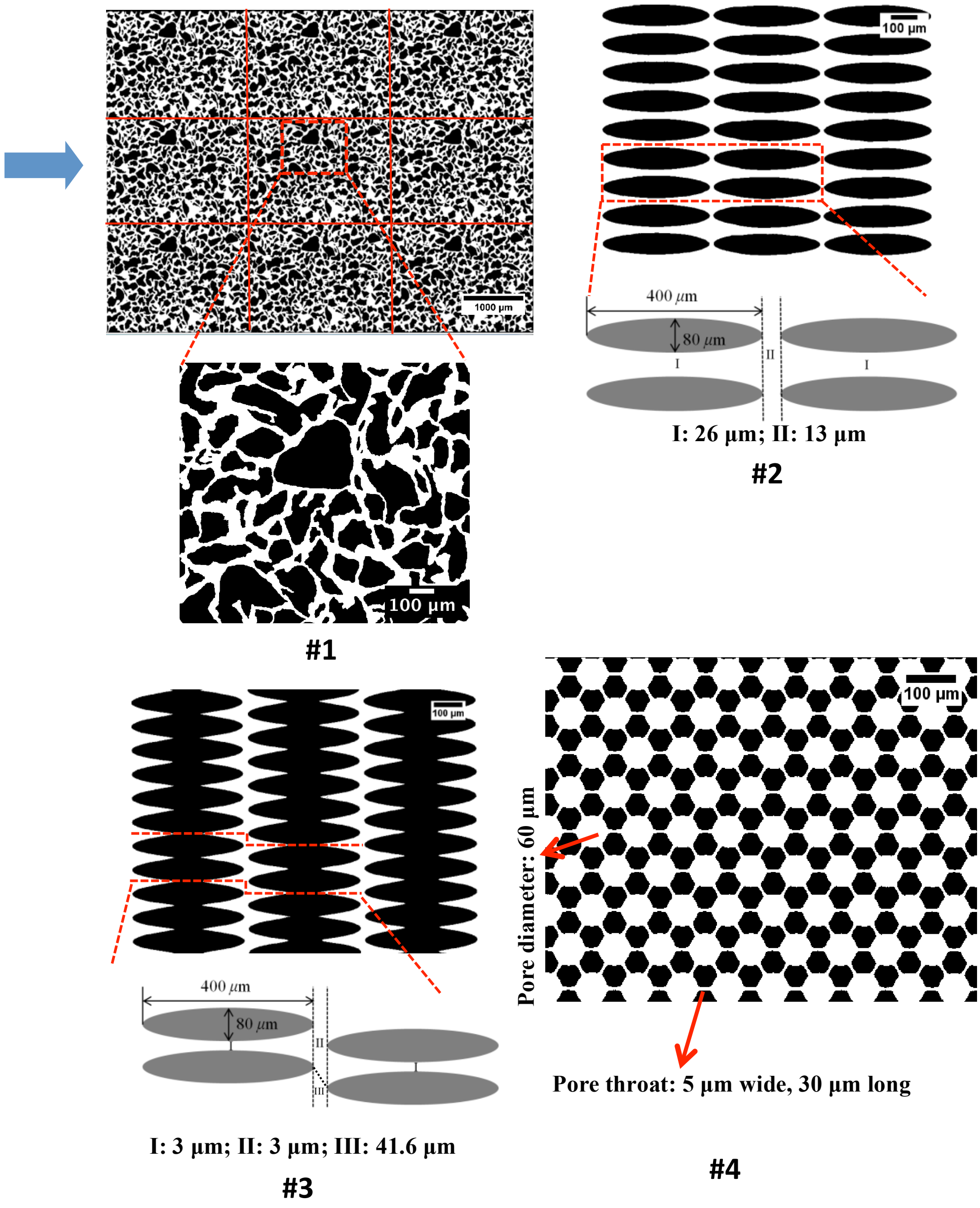
1000 μm
100 μm
#1
100 μm
400 μm
80 μm
I
II
I
I: 26 μm; II: 13 μm
#2
100 μm
400 μm
80 μm
II
III
I: 3 μm; II: 3 μm; III: 41.6 μm
#3
100 μm
Pore diameter: 60 μm
Pore throat: 5 μm wide, 30 μm long
#4

Figure 1

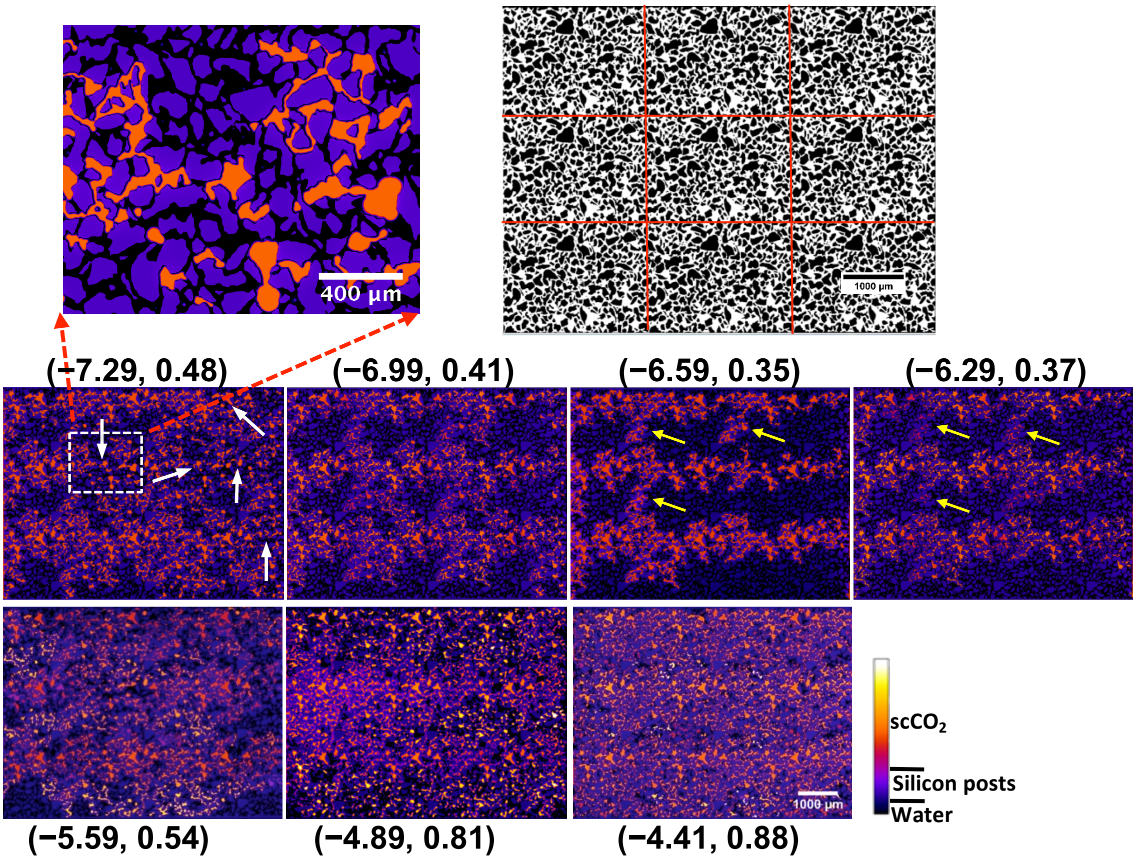
400 µm
1000 µm
(−7.29, 0.48)
(−6.99, 0.41)
(−6.59, 0.35)
(−6.29, 0.37)
1000 µm
scCO$_2$
Silicon posts
Water
(−5.59, 0.54)
(−4.89, 0.81)
(−4.41, 0.88)

Figure 2

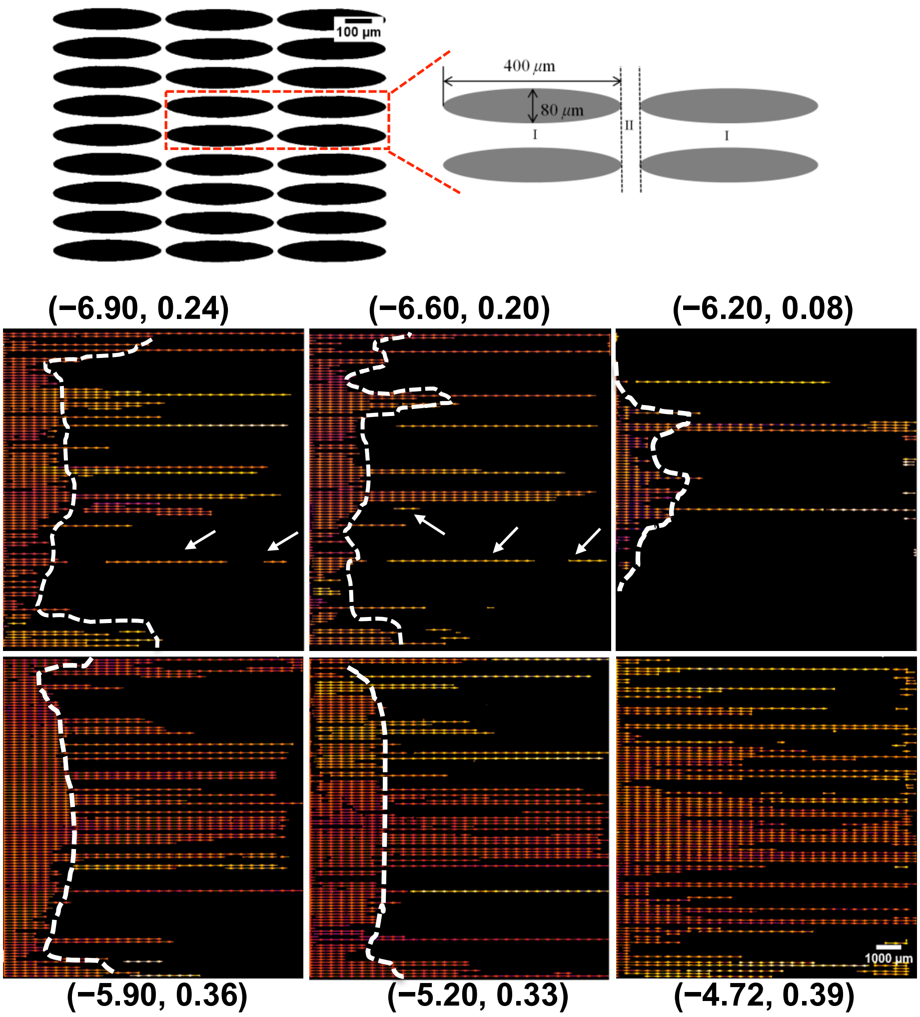

100 μm
400 μm
80 μm
I
II
I
(−6.90, 0.24)
(−6.60, 0.20)
(−6.20, 0.08)
1000 μm
(−5.90, 0.36)
(−5.20, 0.33)
(−4.72, 0.39)

Figure 3

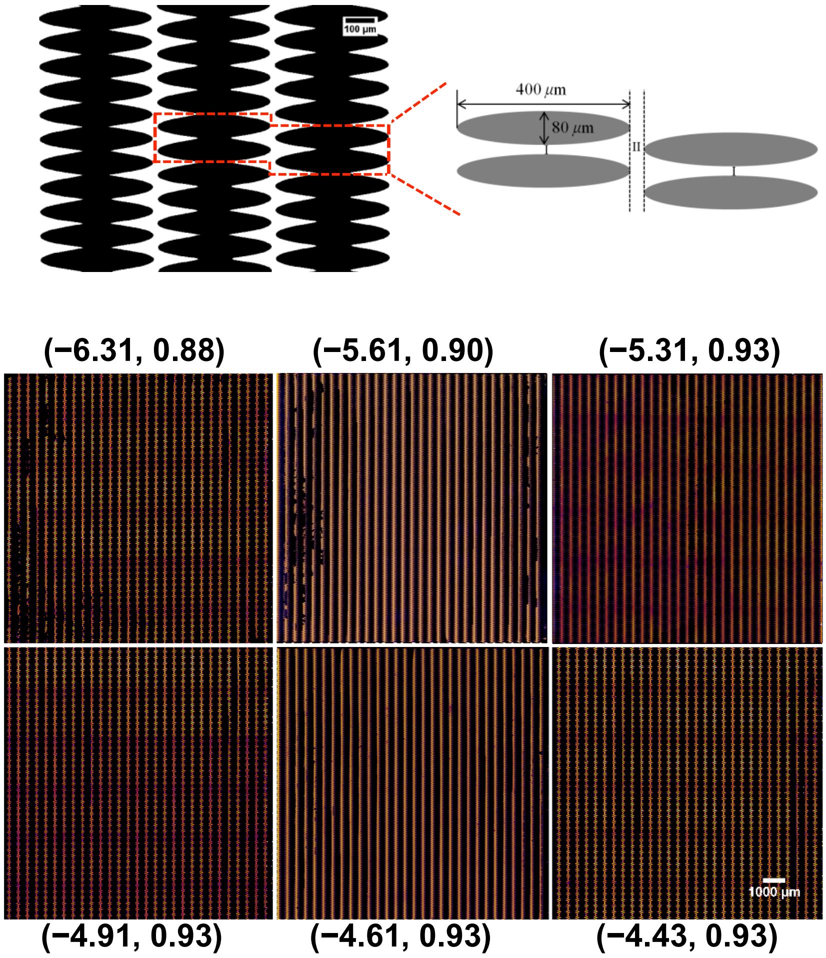
100 µm
400 µm
80 µm
(−6.31, 0.88)
(−5.61, 0.90)
(−5.31, 0.93)
(−4.91, 0.93)
(−4.61, 0.93)
(−4.43, 0.93)
1000 µm

Figure 4

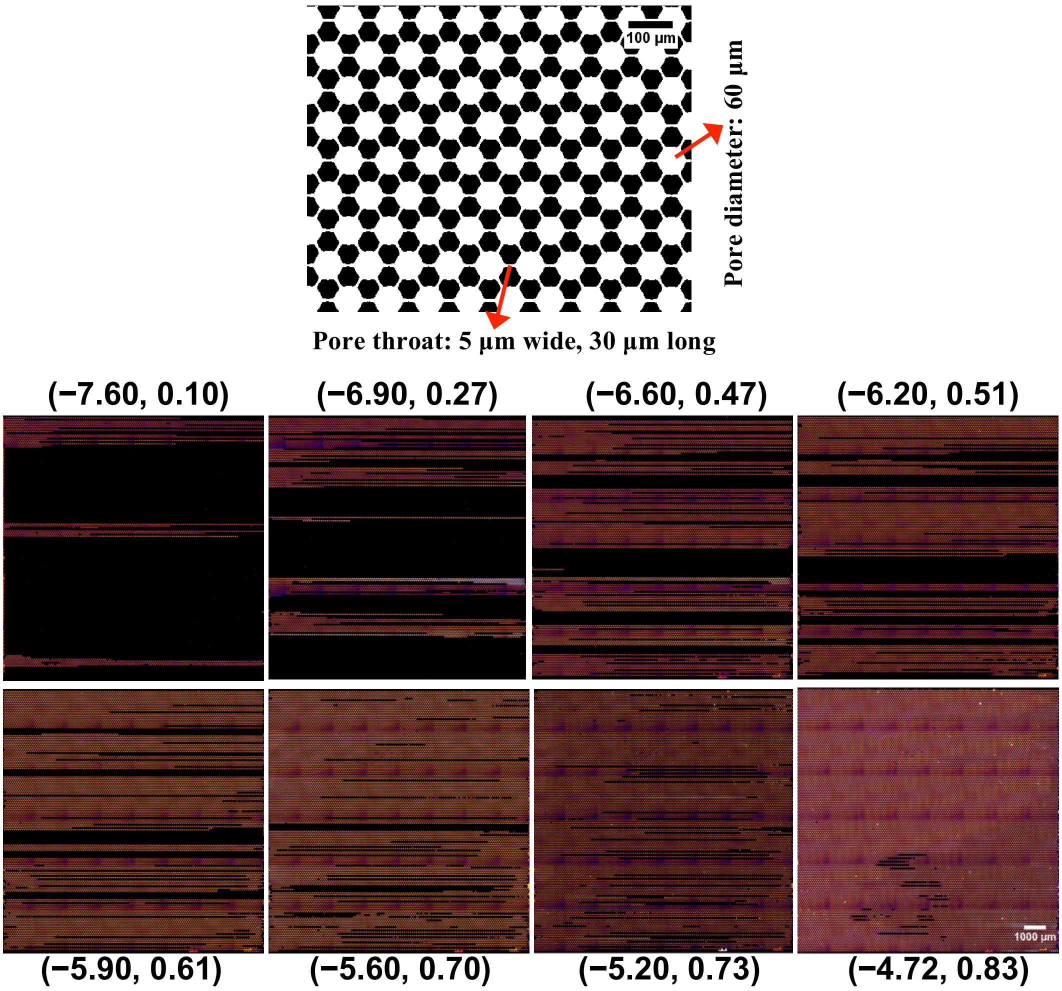
100 µm
Pore diameter: 60 µm
Pore throat: 5 µm wide, 30 µm long
(−7.60, 0.10)
(−6.90, 0.27)
(−6.60, 0.47)
(−6.20, 0.51)
1000 µm
(−5.90, 0.61)
(−5.60, 0.70)
(−5.20, 0.73)
(−4.72, 0.83)

Figure 5

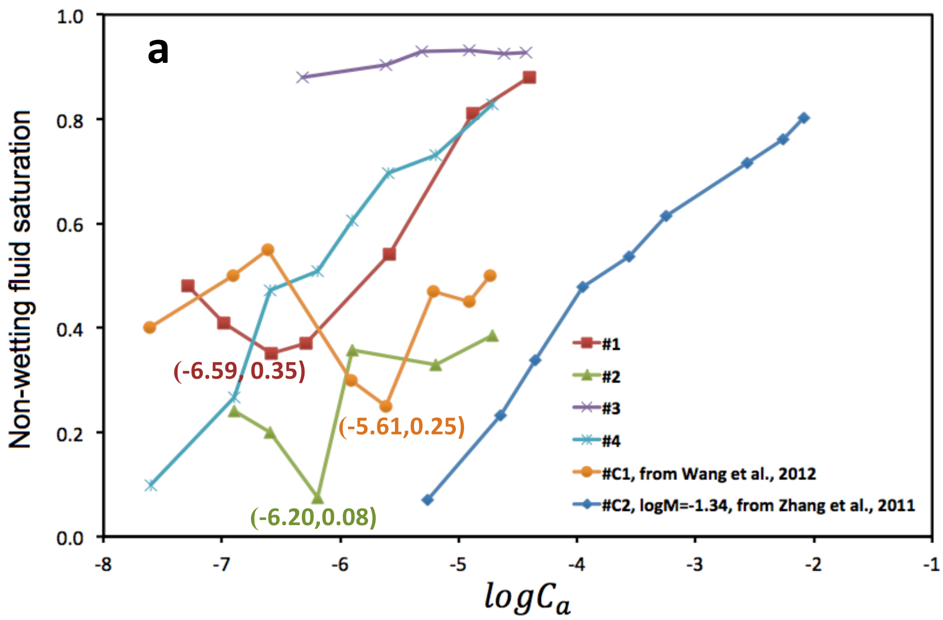

a
Non-wetting fluid saturation
1.0
0.8
0.6
0.4
0.2
0.0
-8
-7
-6
-5
-4
-3
-2
-1
$logC_a$
(-6.59, 0.35)
(-5.61,0.25)
(-6.20,0.08)
#1
#2
#3
#4
#C1, from Wang et al., 2012
#C2, logM=-1.34, from Zhang et al., 2011

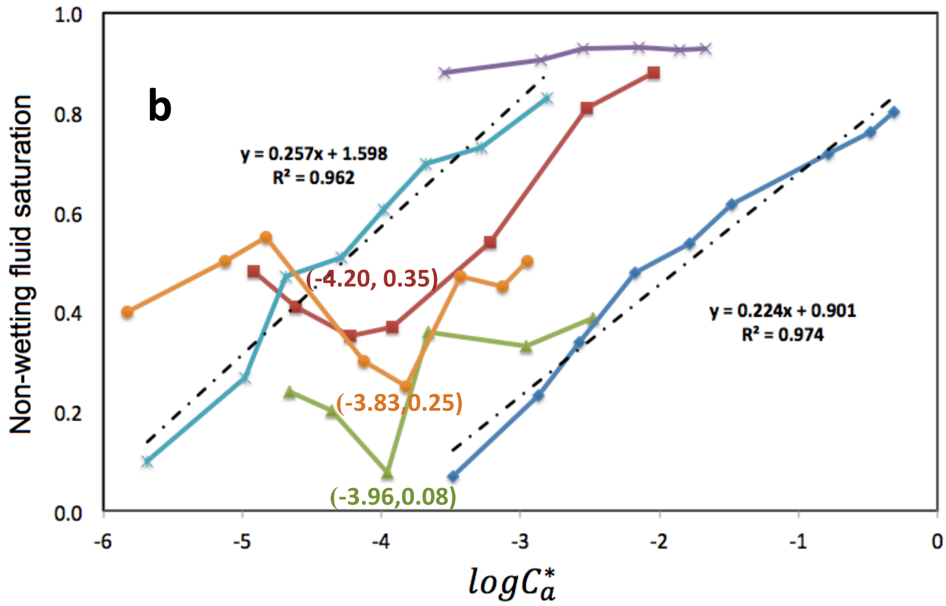

b
Non-wetting fluid saturation
1.0
0.8
0.6
0.4
0.2
0.0
-6
-5
-4
-3
-2
-1
0
$logC_a^*$
y = 0.257x + 1.598
R² = 0.962
y = 0.224x + 0.901
R² = 0.974
(-4.20, 0.35)
(-3.83,0.25)
(-3.96,0.08)

Figure 6

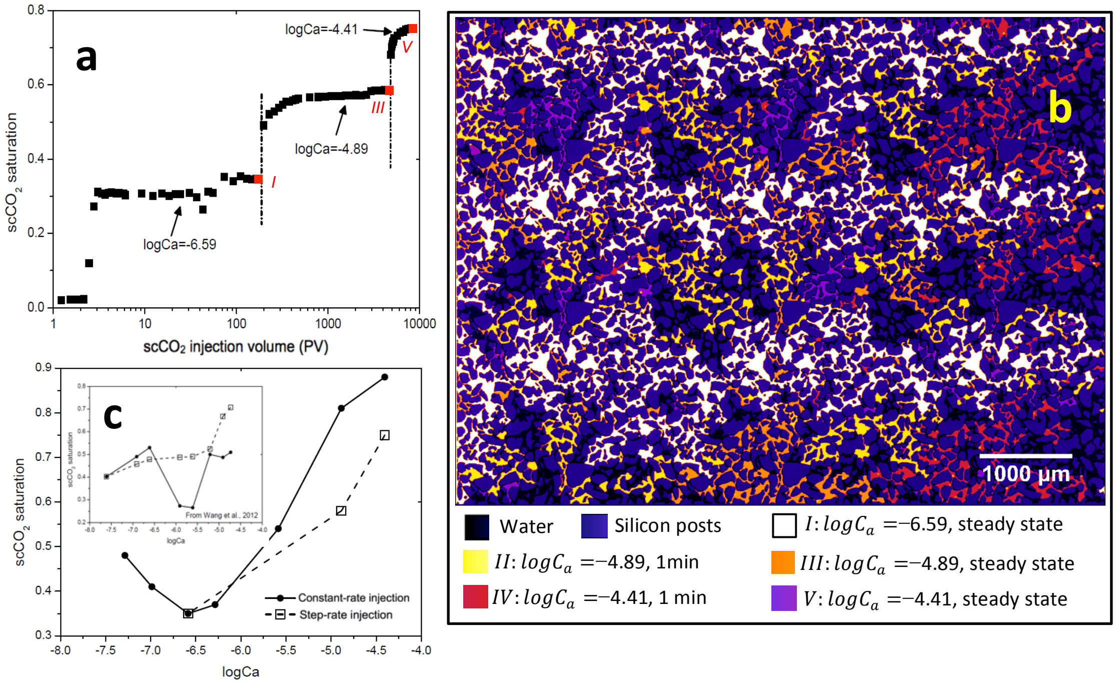
a
logCa=-4.41
V
III
logCa=-4.89
I
logCa=-6.59
scCO2 saturation
scCO2 injection volume (PV)
c
Constant-rate injection
Step-rate injection
From Wang et al., 2012
logCa
b
1000 μm
Water
Silicon posts
I: logCa =−6.59, steady state
II: logCa =−4.89, 1min
III: logCa =−4.89, steady state
IV: logCa =−4.41, 1 min
V: logCa =−4.41, steady state

Figure 7